ADVANCED FUNCTIONAL MATERIALS
www.afm-journal.de

Materials Views
www.MaterialsViews.com

Unusual Photoluminescence of $CaHfO_3$ and $SrHfO_3$ Nanoparticles

Erwan Rauwel, Augustinas Galeckas, Protima Rauwel, and Helmer Fjellvåg*

This article reports on optical properties of $SrHfO_3$ and $CaHfO_3$ nanoparticles with sizes as small as 1.6 nm, synthesized via non aqueous sol–gel routs for the first time. An unexpectedly strong luminescence from the undoped nanoparticles was observed in the visible spectrum over a wide temperature range, also exhibiting sensitivity to temperature variation and surrounding ambient (vacuum/air) and exposure time to UV light. A tentative model is proposed to explain these phenomena in terms of luminescent centers located at the surface of the nanoparticles.

1. Introduction

Perovskite compounds are among the most interesting mixed metal oxide materials in terms of their properties with applications ranging from microelectronics to catalysis.[1] The synthesis of these compounds as nanoparticles is of fundamental importance as size reduction and shape engineering allow modification and tuning of their fundamental properties,[2] thus opening new possibilities for micro-, opto- and nanoelectronic applications.[3] Although this approach has already been proven for many materials,[4] the synthesis of stable perovskite nanoparticles is of great interest in many domains.[5]

$SrHfO_3$ and $CaHfO_3$ perovskite nanoparticles (NPs) as small as 1.6 nm in diameter were synthesized via a non-aqueous sol-gel process (NHSGP) recently developed as an alternative to conventional hydrolytic routes.[6] An important advantage of this method is the possibility to synthesize pure and highly crystalline nano-sized perovskite (ABO_3)-type oxide nanoparticles at low temperatures and without the use of surfactants.[7] $SrHfO_3$ and $CaHfO_3$ are dielectric materials exhibiting a high permittivity. These compounds are optically transparent in the visible range up to deep ultraviolet (UV) but upon doping, for instance with cerium, these perovskite compounds give rise to a new class of transparent optical ceramics.[1d,8] A high melting point (>2400 °C) makes it difficult to synthesize these compounds as single crystals. Nevertheless, these compounds with nearly isotropic optical properties may provide a low cost alternative in devices and in particular when nanoparticles are involved. In this paper, we report on unusual photoluminescence properties of as-synthesized $SrHfO_3$ and $CaHfO_3$ perovskite nanoparticles. The key point is that our undoped perovskite nanoparticles under below-gap excitation conditions are found to emit strong visible luminescence peaking at around 490 nm and 540 nm and exhibiting sensitivity to temperature variation, surrounding ambient (vacuum/air) and exposure to UV light.

In what follows, we present a comparative study of $SrHfO_3$ and $CaHfO_3$ nanoparticles with a primary focus on the latter due to: i) cost-effectiveness of synthesis, ii) strong temperature-dependent photoluminescence, making it a potential candidate for thermal imaging applications and iii) smaller quantities of secondary phases.

2. Structure and Morphology

X-ray diffraction (XRD) and transmission electron microscopy (TEM) studies illustrate that the derived $SrHfO_3$ and $CaHfO_3$ particles take the cubic type crystal structure. XRD analysis shows that an excess of $Ca(OMe)_2$ in the reaction mixture gives a $CaCO_3$ impurity phase with sharp peaks in the diffraction patterns, see Figures 1aS and 1Sb (Supporting Information). Depending on the amount of excess Ca, two situations with secondary phases may occur: formation of a calcite phase in the case of a small Ca-excess (Figure 1bS) or calcite and valerite in the case of large Ca-excess (Figure 1aS). On the other hand, excess of the $Hf(O^tBu)_4$ precursor triggers formation of cubic HfO_2 nanoparticles as a secondary phase. A previous study on the synthesis of HfO_2 nanoparticles using $Hf(O^tBu)_4$ precursor and benzyl alcohol produced monoclinic HfO_2 nanoparticles.[9] However, no monoclinic phase of HfO_2 was detected using XRD measurements or HRTEM, only cubic HfO_2 nanoparticles were observed. The presence of $Ca(OMe)_2$ certainly promoted the production of the cubic phase by substituting Ca at

Dr. E. Rauwel
Department of Chemistry and SFI - inGAP
University of Oslo
P.O. Box 1033 Blindern, 0315 Oslo, Norway
E-mail: erwan.rauwel@kjemi.uio.no
Dr. A. Galeckas
Department of Physics
University of Oslo
P.O. Box 1048 Blindern, 0316 Oslo, Norway
Dr. P. Rauwel
Department of Physics
University of Oslo
Postboks 1048 Blindern, 0316 Oslo, Norway
Prof. H. Fjellvåg
Department of Chemistry and SMN
University of Oslo
Postboks 1033 Blindern, 0315 Oslo, Norway

DOI: 10.1002/adfm.201101013

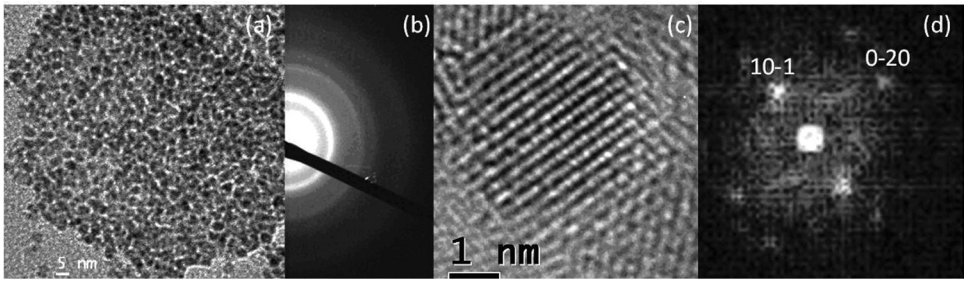

Figure 1. TEM microscopy images of $CaHfO_3$ showing (a) general appearance of these particles, (b) electron diffraction pattern indicating $CaHfO_3$ cubic structure, (c) HRTEM image of a single particle oriented along <110> zone axis and it's FFT (d).

Hf sites in HfO_2.[10] It was difficult to completely eliminate this secondary phase formation during the synthesis and the cubic HfO_2 phase is present in all the samples in non-negligible amounts when compared to the $CaCO_3$ secondary phase. The HfO_2 phase was visible in powder XRD, and also high-resolution TEM could discriminate the cubic HfO_2 nanoparticles (Fm-3m) from the perovskite phase (Pm-3m) as discussed below. The secondary nanophases are expected to influence optical properties of the bulk material, but a previous study established the low response of the cubic HfO_2 phase under UV excitation.[10] Figure 1cS shows a typical XRD pattern of cubic $CaHfO_3$ nanoparticles.

Thermogravimetric (TGA) data for $CaHfO_3$ and $SrHfO_3$ are shown in Figure 2S (Supporting Information) revealing a typical behavior for such method of nanoparticle synthesis.[7] The main difference lies in the weight loss of 1.25% above 600 °C that can be attributed to thermal decomposition of $CaCO_3$[11] in the case of CHO sample (Figure 2aS). This implies that the $CaCO_3$ secondary phase amounts to some 7.9 mol% and $CaHfO_3$ and HfO_2 to 92.1 mol%. The weight loss of 1.43% visible above 600 °C with the SHO sample (Figure 2bS) is due to decomposition of $SrCO_3$ and corresponds to a higher degree of impurities than in the Ca-case; i.e., 13.0 mol% while 87.0 mol% $SrHfO_3$ and HfO_2.

Figures 1a and **Figure 2**a are assemblies of the $CaHfO_3$ and $SrHfO_3$ free standing nanoparticles. The micrographs show that even though the particles are close to each other they are well separated from other particles without any coalescence. Size distribution histograms, Figures 3Sa and 3Sb (Supporting Information), for the compounds provide an average size of 2.3 nm and 3.2 nm for $SrHfO_3$ and $CaHfO_3$, respectively. These values are in good agreement with the particle sizes estimated from the Scherrer's formula as 2 nm for $SrHfO_3$ and 3 nm for $CaHfO_3$, respectively. Moreover, the diffractograms in Figures 1b and 2b clearly show that the particles are randomly oriented. Both diffraction patterns we attributed to cubic structures with the lattice parameters a_{SHO} = 4.06 Å and a_{CHO} = 3.99 Å[12] for $SrHfO_3$ and $CaHfO_3$, respectively. High-resolution TEM images presented in Figures 1c and 2c reveal highly crystalline nanoparticles free of planar defects, such as stacking faults or twinning, and possess the perovkite structure. The corresponding power spectra in Figures 1d and 2d provide the orientation of single particles of Figures 1c and 1d, respectively.

The $CaHfO_3$ nanoparticles were further studied by XPS. **Figure 3**a shows the Ca $2p_{3/2}$ and $2p_{1/2}$ photoelectron peaks. Satisfactory peak fitting is achieved using a $2p_{3/2}/2p_{1/2}$ area ratio of 2/1 and a spin orbit splitting of 3.62 eV. The observed Ca $2p_{3/2}$ peak at 347.0 ± 0.2 eV binding energy (BE) is consistent with Ca^{2+} in perovskites.[13] However, this overlaps completely with the Ca $2p_{3/2}$ peaks expected for calcite and valerite, being reported at 347.1 and 346.9 eV, respectively.[14] The C 1s does not support any major existence of $CaCO_3$ in the studied samples (Figure 4S, Supporting Information). The carbon signal mostly emanates from external contamination as the nanoparticles suspended in ethanol were deposited on a Ar^+ sputter cleaned aluminium foil and were left to dry before introduction into the instrument. The quantification of the elements from the detail scans estimates the amount of Hf, Ca, O and C elements (see **Table 1**) and demonstrates an equal amount of Ca and Hf elements (Ca/Hf = 0.98 ± 0.05) which seems to indicate a very low calcium carbonate content in the sample.

Figure 3b shows the XPS spectra of Hf 4f core levels. Satisfactory peak fitting is achieved using a $4f_{7/2}/4f_{5/2}$ area ratio of 4/3 and a spin orbit splitting of 1.66 eV. The well defined $4f_{7/2}$ peak at 16.6 ± 0.2 BE corresponds to fully oxidized Hf^{4+}.[15] Owing to the correlation between number of valence electrons,

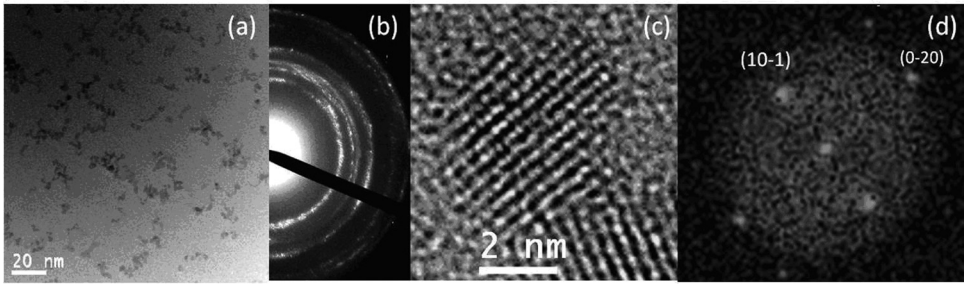

Figure 2. TEM micrographs of $SrHfO_3$ showing (a) general appearance of these particles, (b) electron diffraction pattern indicating $SrHfO_3$ cubic (c) HRTEM image of a single particle oriented along <110> zone axis and it's FFT (d).

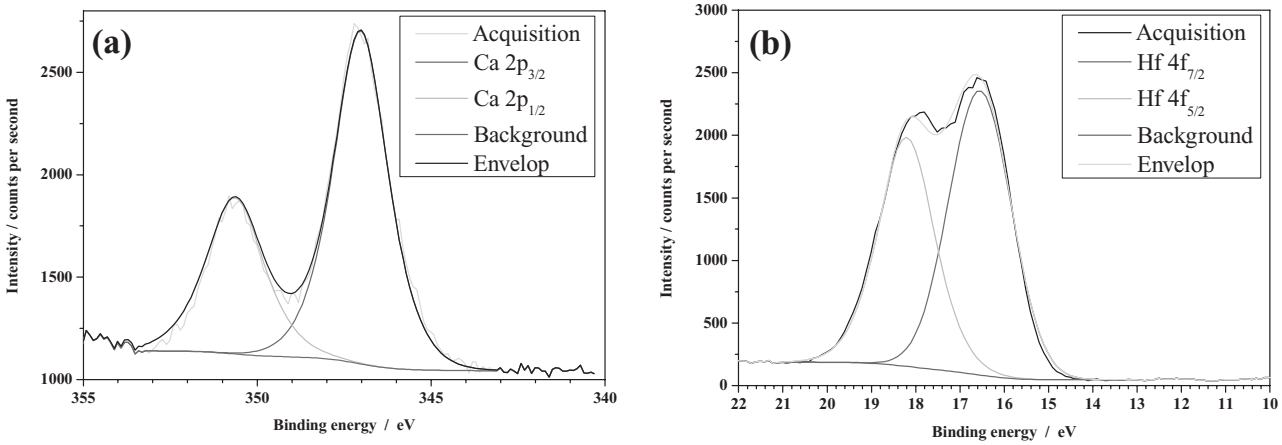

Figure 3. XPS spectra from $CaHfO_3$ nanoparticles dispersed on an aluminium foil. The lines show the deconvoluted (a) Ca 2p and (b) Hf 4f components.

Table 1. Hf, Ca, O, C quantification from XPS results in $CaHfO_3$ nanoparticles.

Element	C1s (C–C)	C1s (O–C=O)	Ca 2p	Hf 4f	O 1s
Percentage (at.%)	31.1	11.6	7.5	7.6	42.2

core electron potentials and binding energy,[16] the lack of shift in the Hf $4f_{5/2}$ and Hf $4f_{7/2}$ peaks, as well as the spin-orbit splitting value of 1.66 eV, shows that hafnium takes the expected oxidation state +4 in the $CaHfO_3$ perovskite nanoparticles or fully oxidized HfO_2 nanoparticles.

3. Optical Characterization

Optical properties of the perovskite nanoparticles were investigated at room temperature by means of UV-visible diffuse-reflectance spectroscopy (DRS). The band gap energies and the dominant type of optical transitions were determined using standard Kubelka–Munk[17] and Tauc[18] treatment of the DRS spectra. The measurements allowed determination of the bandgap of the secondary phase. The absorption edges deduced from DRS for $SrHfO_3$ and $CaHfO_3$ perovskite nanoparticles are summarized in **Figure 4**a, where several prominent absorption sub-thresholds are indicated by arrows. Normalized Tauc plots considering possible involvement of both indirect and direct optical transitions are presented in Figures 4b and 4c, respectively.

3.1. Bandgap

DRS results analized under the assumption of indirect optical transition are presented first. For $SrHfO_3$, the absorption thresholds at 3.6 eV and 4.2 eV correspond to the bandgap of the $SrCO_3$ secondary phase.[19] The bandgap of 4.8 eV could be attributed to the HfO_2 cubic nanoparticles. The presence of the latter was not visible in the powder XRD pattern, but confirmed by TEM. The absorption threshold observed at 6.2eV is considered to be the fundamental bandgap of the $SrHfO_3$ perovskite nanoparticles. In the case of $CaHfO_3$ nanoparticles, three sub-thresholds could be resolved in the absorption spectra. The energy gap of 4.2 eV is attributed to the $CaCO_3$ secondary phase,[20] whereas the optical absorption at 4.8 eV is again associated with the bandgap of HfO_2 cubic nanoparticles. Finally, we consider 6.2 eV as the fundamental optical bandgap of $CaHfO_3$ perovskite nanoparticles. It should be noted that a similar value has been reported for $SrHfO_3$ thin-films by Sousa et al.[21] implying that a particular form of nanostructuring: thin-film or nanoparticle, has no significant

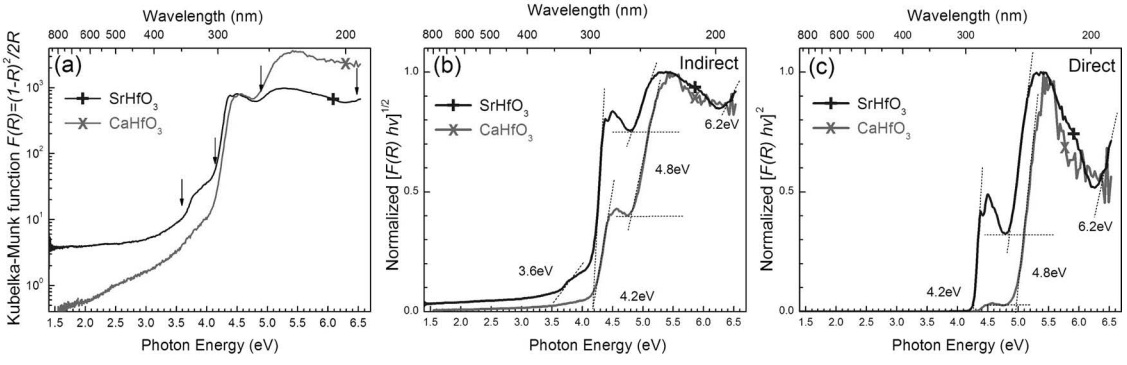

Figure 4. a) Diffuse-reflectance spectra measured in the UV-visible region at 300K for $SrHfO_3$ and $CaHfO_3$ nanoparticles; arrows indicate apparent absorption thresholds. Normalized Tauc plots considering (b) indirect and (c) direct optical transitions for $SrHfO_3$ and $CaHfO_3$.

effect on the fundamental bandgap. To the best of our knowledge, there are no literature reports on the bandgap of bulk $CaHfO_3$.

Analysis of the same DRS data under the assumption of direct optical transitions (see Figure 4c) leads to very similar results, except that the $SrCO_3$ band gap of 3.6 eV is no longer visible, whereas 4.2 eV absorption remains dominant. In the case of the $CaHfO_3$ nanoparticles, only a weak indication of $CaCO_3$ optical band gap can be resolved, suggesting most likely an indirect band gap for this compound.[20] The energy gap at 4.8 eV, which we associate with cubic HfO_2 nanoparticles, appears more prominent in the case of direct transitions. In fact, Jiang et al. recently published that HfO_2 cubic phase has a direct gap along with indirect gaps with close energies.[22] This might explain why this component also fits the indirect bandgap interpretation. The direct fundamental band gaps of $SrHfO_3$ and $CaHfO_3$ are around 6.2 eV, see Figure 4c.

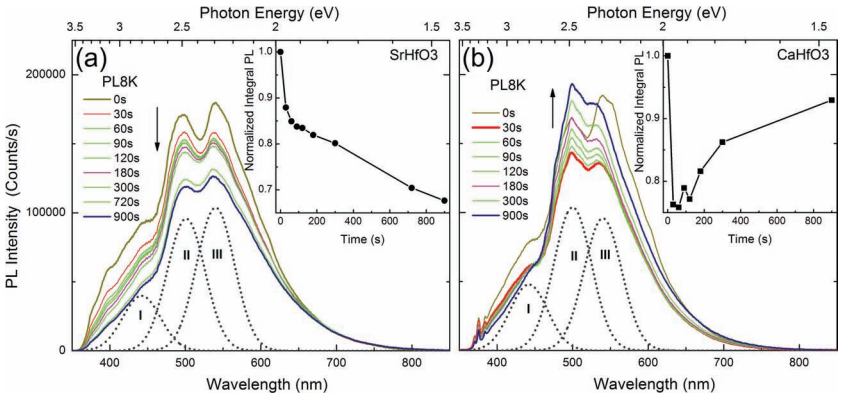

Figure 5. Time evolution of PL spectra upon UV exposure recorded at 8 K for nanoparticles of: a) $SrHfO_3$ and b) $CaHfO_3$. Arrows indicate general trends of the PL yield upon UV-exposure; insets show corresponding evolutions of the integral PL of as function of elapsed time; Gaussian curves indicate the dominant emission components (I, II, III).

3.2. Photoluminescence

Photoluminescence (PL) is a common technique to study structure, defects and impurities in nanocrystals. It is known that upon doping of perovskite nanoparticles with cerium[1d] or europium[23] certain luminescence can be observed from the otherwise optically inactive matrix material. In the present work, we report on PL properties of undoped perovskite nanoparticles under below-gap photo-excitation conditions. The initial measurements performed at room temperature have revealed two important features. Firstly, an unexpectedly strong luminescence in the UV-visible region was observed for both types of NPs. Secondly, spectral instability under continuous UV illumination became immediately apparent, exhibiting different trends for $SrHfO_3$ and $CaHfO_3$ nanoparticles. To get a better insight into these processes, more systematic PL measurements were carried out as a function of temperature (10–300 K), UV-exposure time (0-15 min) and surrounding ambient (air/vacuum).

A comparison of the time evolutions of PL spectra recorded at 8K from $SrHfO_3$ and $CaHfO_3$ nanoparticles under continuous UV-illumination is presented in **Figure 5** with integrated PL intensity versus exposure time dependencies shown as insets. One can readily observe certain similarities in spectral shape and quantum efficiency regardless of the type of NPs. Note, however, the opposite trends in time evolutions: while the luminescence from $SrHfO_3$ nanoparticles steadily decreases, in the case of $CaHfO_3$ the initial abrupt drop of PL intensity is followed by a gradual recovery towards the original level. To simplify the comparative analysis, in what follows we consider only three dominant emission features indicated in Figure 5 as Gaussian components I, II and III at around 2.8, 2.5 and 2.3 eV, respectively.

The effect of the surrounding ambient on the luminescence properties of nanoparticles were deduced from the comparison of room-temperature PL measurements carried out in air and vacuum (10^{-7} Torr) summarized in **Figure 6**. A considerable quenching of the luminescence takes place in air, reducing the integral PL yield to ≈0% and 60% of that in vacuum for $SrHfO_3$ and $CaHfO_3$ NPs, respectively. The green–red spectral region appears particularly susceptible in this respect, i.e., component III is suppressed most in the presence of air, as evidenced by the differential PL spectrum in Figure 6b. The observed dissimilarities in quenching behavior apparently correspond to some intrinsic differences of the surface state of $SrHfO_3$ and $CaHfO_3$ NPs, most likely related to higher affinity of water for calcium than that for strontium element.

4. Discussion

The PL temperature variation may shed light on the origin of the luminescence and dominant recombination mechanisms in nanoparticles. **Figure 7** show PL spectra measured in the temperature range from 10 to 300K for $SrHfO_3$ and $CaHfO_3$ NPs. The corresponding temperature dependencies of the integrated PL are presented in the insets. Although consistent

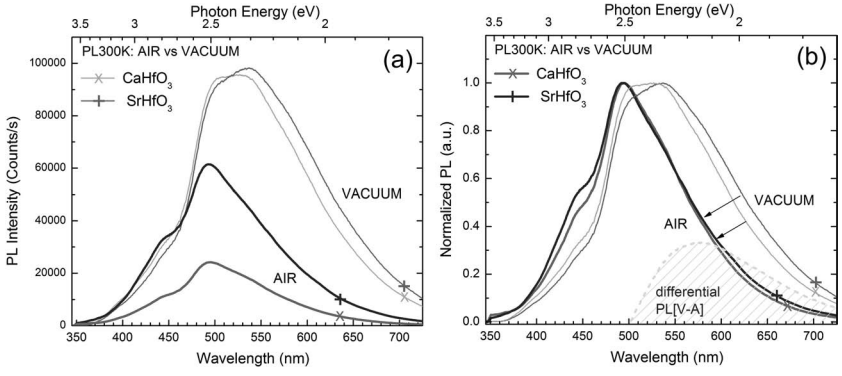

Figure 6. Effects of the surrounding ambient: a) PL spectra measured at 300K in vacuum and air ambient for $SrHfO_3$ and $CaHfO_3$ nanoparticles; b) normalized spectra and differential PL for $CaHfO_3$ (indicated by hatched area).

temperature dependencies appeared intricate to measure because of the UV-instability issues mentioned above, an apparent variation of PL intensity with temperature was revealed for both $SrHfO_3$ and $CaHfO_3$ NPs. While the spectral shape essentially remains unchanged with temperature, a peculiar increase of the integral PL intensity can be observed in a narrow temperature range around 175 K for both type of nanoparticles, even though to a smaller degree in the case of $SrHfO_3$. Such a temperature behavior resembles a well known feature in classic description of the quantum yield of nanocrystals, which assumes competition between radiative recombination and non-radiative hopping processes.[24] Analytically, this can be described as $I(T) = I_0/(1 + \nu_0 \exp[T/T_B + T_r/T])$, where ν_0 is reduced frequency parameter, T_r is a characteristic activation temperature pertaining to the radiative recombination, and T_B the characteristic Berthlot temperature associated with the non-radiative escape (hopping) processes. Accordingly, the maximum of PL intensity is expected at temperature $T_m = (T_r\ T_B)^{½}$ as a result of competition of Arrhenius type radiative process $R_r = \nu_r \exp[T_r/T]$ and non-radiative hopping $R_{hop} = \nu_B \exp\ [T/T_B]$. The decrease of PL intensity at lower temperatures (in our case at $T < 175$ K) then could be associated with tunneling of carriers from the NPs to non-radiative centers, which is possible due to long radiative lifetimes at low T. The maximum in the temperature dependence of PL occurs at some specific temperature determined mainly by the crystallite size. This fact would explain the same $T_m = 175$ K for both $SrHfO_3$ and $CaHfO_3$ NPs, which are virtually of the same size. At yet higher temperatures, the radiative transitions start to overwhelm the non-radiative tunneling process and, since total PL intensity is governed by the combination of these radiative and non-radiative processes, a characteristic peak is expected to show up in the temperature dependence of the PL intensity.

Finally, we address the possible origin of the surprisingly strong luminescence from $SrHfO_3$ and $CaHfO_3$ nanoparticles taking into account the 3.8 eV photon energy of excitation used in the present experiments, which is neither sufficient for interband generation of electron–hole pairs, nor any substantial contribution could be expected from several absorption sub-thresholds observed below the fundamental gap at ≈3.6/ 4.2/ 4.8 eV (see Figure 4).

It should be noted that secondary phases, especially if present in considerable amounts, might contribute to the PL emission However, there are several proven ways of suppressing or reducing the secondary phases viz. regulating the synthesis temperature or varying the Ca(Sr)/Hf ratio. An even more reductive precursor is currently being employed for eliminating the secondary phases and will be reported separately in future articles. According to literature reports, the high-energy shoulder in PL spectra around 3.2 eV could be associated with the $CaCO_3$ secondary phase,[20] whereas $SrCO_3$ would contribute in a wider spectral range with a maximum at around 2.36 eV (525 nm).[19] Although involvement of some residual amounts of $CaCO_3$ and $SrCO_3$ can not be ruled out, the share magnitude of the luminescence suggests some alternative sources. Indeed, it is well known that characteristic luminescence commonly observed from nanocrystals in the range 350–550 nm (2.2–3.5 eV) actually originates from defects located on the surface of a particle. The huge surface-to-volume SA/V ratio of the nanoparticles studied in the present work ($SA/V = 3/r \approx 10^9$) suggests possible accumulation of a large number of defects on the particle surface, thus it is reasonable to assume that the origin of the intense visible luminescence from $SrHfO_3$ and $CaHfO_3$ is entirely interfacial. Besides providing luminescent centers, surface localized states are also known to act as non-radiative centers and thus are capable of shaping the entire luminescence process on their own. This kind of interfacial model would readily explain the observed sensitivity of PL spectral shape and intensity to surrounding ambient (air/vacuum) as well as to UV exposure. The likely cause of the variable luminescence efficiency is so called hydroxyl quenching, which occurs once the electronic structure of nanoparticles is perturbed by OH or $(OH)_2$ radicals adsorbed on the surface.[25] This effect is commonly reported for nanoparticles suspended in water and thus can also be anticipated in naturally wet air ambient. Consequently, our measurement results can be understood in terms of water splitting under UV-excitation, which in turn would facilitate hydroxyl-quenching of the luminescence. On the other hand, different surface charge state of the neighboring NPs might provide yet another mechanism for the observed optical instability under UV excitation, given that it can directly influence the aforementioned electron hopping and thus affect the non-radiative recombination rate.

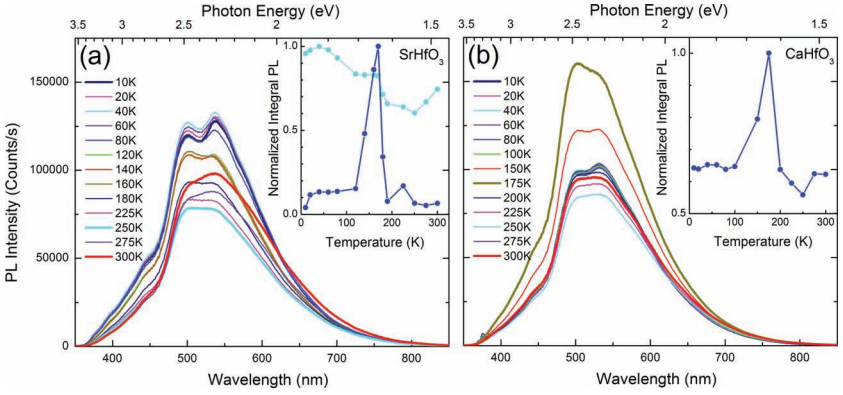

Figure 7. Temperature-dependent PL spectra of (a) $SrHfO_3$ nanoparticles (b) $CaHfO_3$ nanoparticles; insets show corresponding evolutions of the integral PL yield as a function of temperature. Note that for $SrHfO_3$, the actual temperature variation is represented by inclined upper curve, whereas the local peak is obtained upon baseline subtraction.

5. Conclusions

In conclusion, $SrHfO_3$ and $CaHfO_3$ nanoparticles as small as 1.6 nm in diameter were synthesized using a non-aqueous sol–gel approach. We demonstrate that these undoped perovskite materials, known to be optically inactive in the form of bulk compounds and thin films, exhibit strong visible luminescence upon nanostructuring. The observed variation of PL with temperature, sensitivity to surrounding ambient (vacuum/air) and exposure time to UV light suggest surface-related origin of the luminescence centers, while huge surface-to-volume ratio of the investigated nanoparticles is considered as the key factor of high quantum

efficiency. In addition, UV–visible diffuse reflectance measurements allowed for the detection of impurity phases and determination of optical band gaps of the $CaHfO_3$ and $SrHfO_3$ nanoparticles, and for the first time the optical band gap of $CaHfO_3$ was determined experimentally. These nanoparticles are now being integrated into devices engineered for thermal imaging applications and will be the subject of future communications.

6. Experimental Section

Synthesis: The procedure for synthesizing $SrHfO_3$ and $CaHfO_3$ nanoparticles is as follows: The synthesis procedures were carried out in a glove box (O_2 and $H_2O < 1$ ppm). In a typical synthesis, metallic strontium (1.78 mmol) (Sr metal dendritic pieces (99.9%), Aldrich) or calcium methoxide (1.74 mmol) (Ca methoxide (97%), Aldrich) were added to 20 mL (193 mmol) benzyl alcohol (Benzyl alcohol (99%), Aldrich). Once the solution clarifies (stirring at around 60 °C is needed to dissolve the strontium metal or calcium methoxide) hafnium (IV) tert-butoxide (1.79 and 1.74 mmol, respectively) (Hafnium tert-butoxide 99.9%, STREM) was added. The reaction mixture was transferred into a stainless steel autoclave and carefully sealed. Thereafter, the autoclave was taken out of the glove box and heated in a furnace at 300 °C for 2 days. The resulting milky suspensions were centrifuged, the precipitates thoroughly washed with ethanol and dichloromethane and subsequently dried in air at 60 °C.

Characterization: X-ray diffraction (XRD) patterns were collected using a Philips X'Pert powder diffractometer equipped with a Cu Kα_1 radiation source (λ = 0.15406 nm). High-resolution transmission electron microscopy (HRTEM) was carried out on a JEOL-2010F transmission electron microscope operated at 200 kV. X-ray photoelectron spectroscopy analyses were carried out on a Kratos Analytical Axis Ultra^{DLD} photoelectron spectrometer equipped with a monochromated Al Kα X-ray source. Thermogravimetric (TG) analyses were carried out in flowing O_2 atmosphere (15 mL min^{-1}) with a heating rate of 5 °C min^{-1}, using a Rheometric Scientific STA 1500 instrument.

Optical absorption properties were derived from the diffuse reflectance measurements performed at room temperature using ThermoScientific EVO-600 UV-VIS spectrophotometer. PL was investigated in the temperature range from 10 K to 300 K by employing 325 nm wavelength of cw He-Cd laser with an output power of 10mW as an excitation source. The emission was collected by a microscope and directed to fiber optic spectrometer (Ocean Optics USB4000, spectral resolution 2nm). Temperature-dependent measurements were realized using closed-cycle He-refrigerator (Janis, Inc. CCS450).

Supporting Information

Supporting Information is available from the Wiley Online Library or from the author.

Acknowledgements

We thank Mrs. S. Aravinthan for her assistance with the TGA and TDA measurements and Mr. M. F. Sunding for XPS analyses. We thank Dr. Mohamed Karmaoui for the synthesis of $SrHfO_3$ sample and fruitful discussion. Financial support from Research Council of Norway for financial support, project 176740/130 and Marie Curie (PERG05-GA-2009-249243) is acknowledged.

Received: May 6, 2011
Revised: June 23, 2011
Published online: September 9, 2011

[1] a) C. H. Ahn, K. M. Rabe, J.-M. Triscone, *Science* **2004**, *303*, 488; b) J. M. D. Coey, M. Viret, S. von Molnar, *Adv. in Physics* **1999**, *48*, 167; c) W. Prellier, M. P. Singh, P. Murugavel, *J. Phys.: Condens. Matter* **2005**, *17*, R803; d) Y. M. Ji, D. Y. Jiang, Z. H. Wu, T. Feng, J. L. Shi, *Mater. Res. Bull.* **2005**, *40*, 1521; e) J. G. Bednorz, K. A. Müller, *Rev. Mod. Phys.* **1988**, *60*, 585; f) S. Han, L. C. DeCaul, R. E. Palermo, D. E. Walsh, *US Patent 5,149,516*, 1992.

[2] *Properties and Applications of Perovskite Type Oxides*; (Eds: L. J. Tejuca, J. L. G. Fierro), Marcel Dekker, New York, **1993**.

[3] C. Dubourdieu, I. Gélard, O. Salicio, G. Saint-Girons, B. Vilquin, G. Hollinger, *Int. J. Nanotechnol.* **2010**, *7*, 320.

[4] N. Pinna, G. Neri, M. Antonietti, M. Niederberger, *Angew. Chem. Int. Ed.* **2004**, *43*, 4345.

[5] a) N. X. Phuc, H. M. Nguyen, D. H. Manh, L. T. Hung, L. T. C. Tuong, L. V. Hong, Y.-D. Yao, *J. Magn. Magn. Mater* **2006**, *304*, 133; b) B. A. Hernandez-Sanchez, T. J. Boyle, C. M. Baros, L. N. Brewer, T. J. Headley, D. R. Tallant, M. A. Rodriguez, B. A. Tuttle, *Chem. Mater.* **2007**, *19*, 1459; c) X.-L. Yu, Y. Wang, Y.-M. Hu, C.-B. Cao, H. L.-W. Chan, *J. Am. Ceramic Soci.* **2009**, *92*, 3105; d) S. Farhadi, N. Rashidi, *Polyhedron* **2010**, *29*, 2959; e) R. Epherre, E. Duguet, S. Mornet, E. Pollert, S. Louguet, S. Lecommandoux, C. Schatz, G. Goglio, *J. Mater. Chem.* **2011**, *21*, 4393.

[6] a) A. Vioux, *Chem. Mater.* **1997**, *9*, 2292; b) M. Niederberger, G. Garnweitner, N. Pinna, M. Antonietti, *J. Am. Chem. Soc.* **2004**, *126*, 9120; c) M. Niederberger, N. Pinna, J. Polleux, M. Antonietti, *Angew. Chem. Int. Ed.* **2004**, *43*, 2270.

[7] M. Niederberger, N. Pinna, *Metal Oxide Nanoparticles in Organic Solvents: Synthesis, Formation, Assembly, and Application*, Springer, **2009**.

[8] E. V. van Loef, W. Higgins, J. Glodo, C. Brecher, A. Lempicki, V. Venkataramani, W. W. Moses, S. E. Derenzo, K. S. Shah, *IEEE Nuclear Science Symp. Conf. Rec.* **2006**, 1538.

[9] N. Pinna, G. Garnweitner, M. Antonietti, M. Niederberger, *Adv. Mater* **2004**, *16*, 2196.

[10] A. Pucci, G. Clavel, M.-G. Willinger, D. Zitoun, N. Pinna, *J. Phys. Chem. C* **2009**, *113*, 12048.

[11] E. Oniyama, P. G. Wahlbeck, *Thermochim. Acta* **1995**, *250*, 41.

[12] A. López-García, R. E. Alonso, M. Falabella, G. Echeverría, *Ferroelectrics* **2008**, *363*, 50.

[13] a) P. A. W. van der Heide, *Surf. Sci.* **2001**, *490*, L619; b) X. Y. Qiu, H. W. Liu, J. Fang, M. J. Ha, X. H. Zhou, J.-M. Liu, *Appl. Phys. A* **2005**, *81*, 1431.

[14] C. S. Gopinath, S. G. Hegde, A. V. Ramaswamy, S. Mahapatra, *Mater. Res. Bull.* **2002**, *37*, 1323.

[15] D. D. Sarma, C. N. R. Rao, *J. Electron Spectrosc. Relat. Phenom.* **1980**, *20*, 25.

[16] P. S. Bagus, F. Illas, G. Paccghioni, F. Parmigiani, *J. Electron Spectrosc. Relat. Phenom.* **1999**, *100*, 215.

[17] P. Kubelka, F. Munk, *Z. Tech. Phys.* **1931**, *12*, 593.

[18] J. Tauc, R. Grigorovici, A. Vancu, *Phys. Status Solidi* **1966**, *15*, 627.

[19] S. Ni, X. Yang, T. Li, *Mater. Lett.* **2011**, *65*, 766.

[20] S. K. Medeiros, E. L. Albuquerque, F. F. Maia Jr., E. W. S. Caetano, V. N. Freire, *J. Phys. D: Appl. Phys.* **2007**, *40*, 5747.

[21] M. Sousa, C. Rossel, C. Marchiori, H. Siegwart, D. Caimi, J. P. Locquet, D. J. Webb, R. Germann, J. Fompeyrine, K. Babich, J. W. Seo, C. Dieker, *J. Appl. Phys.* **2007**, *102*, 104103.

[22] H. Jiang, R. I. Gomez-Abal, P. Rinke, M. Scheffler, *Phys. Rev. B* **2010**, *81*, 085119.

[23] A. Dobrowolska, E. Zych, *Chem. Mater.* **2010**, *22*, 4652.

[24] G. C. John, V. A. Singh, *Phys. Rev. B* **1966**, *54*, 4416.

[25] E. Konstantinova, J. Weidmann, T. Dittrich, *J. Porous Mater.* **2000**, *7*, 389